Chapter 18

Reaction Kinetics and Simulation of Growth in Pyrolytic Laser-Induced Chemical Vapor Deposition

D. Bäuerle, N. Arnold, and R. Kullmer

Angewandte Physik, Johannes-Kepler-Universität Linz, A–4040 Linz, Austria

This overview summarizes model calculations on the gas-phase kinetics and the simulation of growth in pyrolytic laser-induced chemical vapor deposition. The theoretical results are compared with experimental data.

*L*aser-induced *c*hemical *v*apor *d*eposition (LCVD) permits the single-step production of microstructures and the fabrication of thin extended films. An overview on the various possibilities of this technique, on the different systems investigated, and on the experimental arrangements employed is given in (*1*).

The decomposition of precursor molecules employed in laser-CVD can be activated mainly thermally (photothermal or pyrolytic LCVD) or mainly non-thermally (photochemical or photolytic LCVD) or by a combination of both (hybrid LCVD). The type of process activation can be verified from the morphology of the deposit, from measurements of the deposition rate as a function of laser power, laser wavelength, substrate material etc. and, last not least, from the analysis of data on the basis of theoretical models.

In this chapter we concentrate on the analysis of the reaction kinetics and the simulation of growth in *pyrolytic* laser-CVD of microstructures.

Photochemical laser-CVD based on selective electronic excitations has also been applied for the fabrication of microstructures (*1*). Nevertheless, the main importance of this technique is found in the field of thin film fabrication.

This chapter is organized as follows: We start with a few remarks on precursor molecules (Sect. 1) and on the type of microstructures fabricated by pyrolytic LCVD (Sect. 2). In Sect. 3 we discuss different theoretical approaches for the description of the gas-phase kinetics in pyrolytic LCVD of microstructures. The simulation of growth on the basis of one-dimensional and two-dimensional models is treated in Sect. 4. While we concentrate on a few model systems for

0097–6156/93/0530–0250$06.75/0

which the most complete data are available, the discussion of results is very general in the sense that most of the trends, features and results apply to all the corresponding systems that have been studied. The investigations presented are of relevance to both the application of laser-CVD in micro-patterning and the elucidation of the fundamental mechanisms in laser micro-chemistry.

1. Precursor Molecules

The precursor molecules most frequently employed in laser-CVD are halogen compounds, hydrides, alkyls, carbonyls, and various organometallic coordination complexes.

For the application of laser-CVD in micro-patterning, the proper selection of precursor molecules is of particular importance. Halogen compounds and hydrides require, in general, higher temperatures for thermal decomposition than organic molecules. In photolytic LCVD, organic precursors permit a greater flexibility in the sense that it is easier to find a precursor molecule which matches the requirements for high yield photodecomposition at the available laser wavelength. On the other hand, utilization of organic precursors is often linked with the incorporation of large amounts of impurities into the deposit, in particular of carbon. Such impurities deteriorate the physical and chemical properties of the deposited material. Thus, the various precursor molecules and the different activation mechanisms for decomposition all have their specific advantages and disadvantages (*1*).

2. Types of deposits

The fabrication of microstructures by pyrolytic laser-CVD has been investigated for spots, rods and stripes (*1*). In such experiments, a semi-infinite substrate is immersed in a reactive gaseous ambient and perpendicularly irradiated by a laser beam. Henceforth, we assume that the laser light is exclusively absorbed on the surface of the substrate or on the already deposited material. The laser-induced temperature rise on this surface heats also the adjacent gas phase. Thus, laser radiation can photothermally activate a reaction of the type

$$\zeta_{AB}\ AB + \zeta_C\ C + M \underset{k_2}{\overset{k_1, k_3}{\rightleftarrows}} \zeta_A\ A(\downarrow) + \zeta_{BC}\ BC + M \qquad (2.1)$$

where ζ_j are stoichiometric coefficients which can depend on the particular reaction path. The forward reaction between AB and C can take place heterogeneously at the gas-solid interface and/or homogeneously within the gas phase just above the irradiated substrate surface. The surface and gas-phase forward reactions shall be characterized by the rate constants k_1 and k_3, respectively. M is an inert carrier gas. A and BC are products of the forward reaction. A shall be the relevant species for surface processing. If A is generated in the gas phase, it must first diffuse to reach the substrate surface to be processed. Species A can just stick on the

surface and form a deposit or it can react further. In the backward reaction, condensed species A react with BC to form the original constituents. This backward reaction is characterized by k_2. For thermally activated reactions, the rate constants can be described by an Arrhenius law $k_j(T) = k_{oj} \exp\{-\Delta E_j/[k_B T]\}$.

We now consider some practical cases. Assume the reaction (2.1) describes the laser-induced chemical vapor deposition of tungsten according to

$$WF_6 + 3H_2 + M \underset{k_2}{\overset{k_1, k_3}{\rightleftarrows}} W(\downarrow) + 6HF + M \qquad (2.2)$$

This process has been studied in great detail. Figure 1 shows different types of W spots deposited according to (2.2) by means of Ar^+-laser radiation. The spot shown in Figure 1*a* is well *localized* and surrounded by a transparent ring and a very thin film (see Figure 1a'). Spots of the type shown in Figure 1*c* are very flat and have a *diffuse* shape. They are also surrounded by a thin film. Spots of the type shown in Figure 1*b* represent an intermediate situation. At fixed laser power, P, and laser-beam illumination time, τ_ℓ, the shape of spots depends on the ratio of partial pressures $p^+ = p(H_2)/p(WF_6)$. On the other hand, if p^+ and τ_ℓ are fixed, the shape of spots changes with increasing power from the 1*a* via the 1*b* to the 1*c* type.

Another practical example is the deposition and etching of Si according to

$$SiCl_4 \underset{k_2}{\overset{k_1, k_3}{\rightleftarrows}} Si(\downarrow) + 2Cl_2 \qquad (2.3)$$

In this reaction one can add H_2 and/or an inert gas as well. If the chemical equilibrium is shifted to the left side, (2.3) describes the etching of Si in Cl_2 atmosphere (*1*).

With the saturation of growth in spot diameter, the continuation of laser-beam irradiation can result in the growth of a rod along the laser-beam axis. This has been described in detail in (*1*).

If the laser beam is scanned with respect to the substrate, one can directly write lines, or complicated patterns. Examples for direct writing can be found in (*1*).

3. Gas-phase Kinetics, Heterogeneous and Homogeneous Reactions

The models employed for investigating the gas-phase kinetics in pyrolytic LCVD are shown in Figures 2 and 3. The reaction zone is either represented by a hemisphere or by a thin circular film placed on a semiinfinite substrate. The hemispherical model is particularly suited to investigate different types of gas-phase transport processes. The cylindrical model, on the other hand, permits to

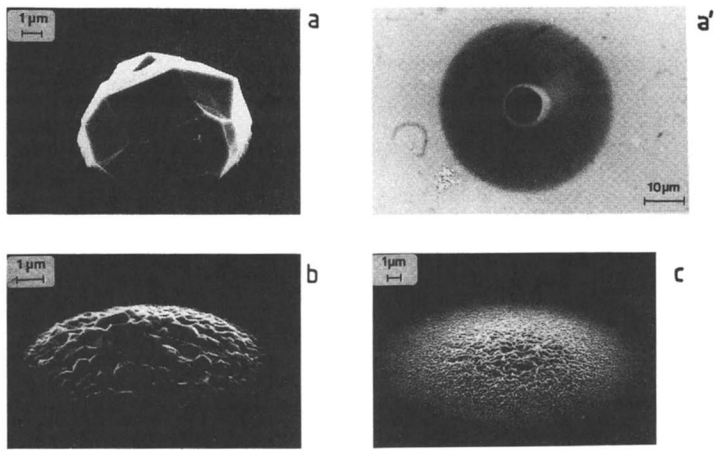

Figure 1. Scanning electron microscope (SEM) pictures (a-c) and optical transmission microscope picture (a') of W spots deposited from a mixture of WF_6 and H_2 on fused quartz (SiO_2) substrates by means of Ar^+-laser radiation (λ = 514.5 nm, $w_o(1/e) \approx 1.1$ µm). a,a') P = 120 mW, τ_ℓ = 0.2 s, p^+ = 2 [10/5 ≡ 10 mbar H_2 + 5 mbar WF_6] b) P = 110 mW, τ_ℓ = 0.5 s, p^+ = 5 [25/5] c) P = 120 mW, τ_ℓ = 0.5 s, p^+ = 50 [250/5] (Reproduced with permission from reference 2. Copyright 1992 Springer-Verlag).

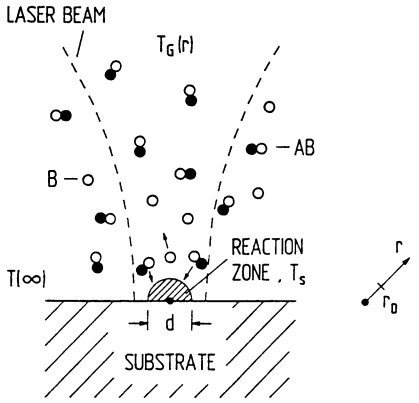

Figure 2. Schematic for laser-induced pyrolytic processing. The reaction zone is represented by a hemisphere of radius $r_D = d/2$ whose surface temperature, T_s, is uniform. The gas-phase temperature is $T_G(r)$. The origin of the radius vector r is in the center of the hemisphere. The laser radiation is exclusively absorbed on the surface $r = r_D$. Carrier gas molecules, being possibly present, are not indicated.

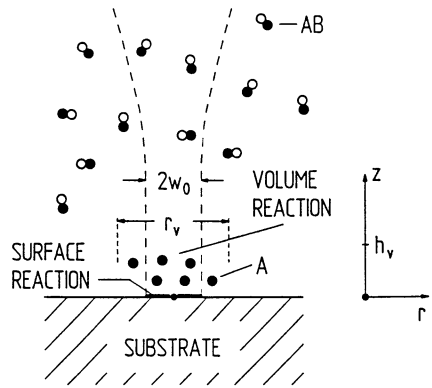

Figure 3. Schematic for pyrolytic laser-induced chemical processing. The origin of the coordinate system is on the substrate surface in the center of the laser beam. The laser light is exclusively absorbed on the surface z = 0. The temperature distributions on the surface z = 0 and in the gas-phase are $T_s(r)$ and $T(r,z)$, respectively (Reproduced with permission from reference 6. Copyright 1992 Elsevier Sequoia).

include, in a simple way, the effect of volume reactions and to describe qualitatively the shape of deposits.

In the model shown in Figure 2 we assume the temperature of the hemisphere (deposit) to be uniform and the reaction to be purely heterogeneous. The reaction rates can then be calculated analytically with respect to temperature- and concentration-dependent transport coefficients, and with respect to the effect of thermal diffusion and chemical convection. The results were published in (*3-5*). These results permit to explain qualitatively many features observed in pyrolytic laser-CVD. One example is the effect of thermal diffusion, that has been studied experimentally during steady-growth of carbon rods deposited from pure C_2H_2 and from admixtures with H_2, He, and Ar. For further details the reader is referred to (*1,3*). The calculations elucidate the relative importance of single contributions to the reaction rate, and also reveal new effects that originate from the coupling of fluxes (*5*).

With the model shown in Figure 3, the influence of heterogeneous *and* homogeneous contributions to the reaction flux has been calculated (*6*). This model certainly applies to "flat" structures only. Nevertheless, the solutions help to interpret processing profiles observed in laser-CVD and laser-chemical etching. Let us consider a reaction of the type (2.1) and discuss only the most general case which must in fact be considered with reactions (2.2) and (2.3). Figure 4 shows only a few of the many different shapes that can be obtained in such a situation. Here, we have plotted the normalized particle flux, $-J^*(r^*)$, which is proportional to the reaction rate, $W^*(r^*)$. At lower center temperatures than those shown in the figure, the maximum reaction flux appears in the center of the laser beam at $r^* = 0$ and thus the thickness of the deposit decreases monotoneously with distance r^*. Above a certain center temperature, however, the maximum reaction flux may occur at a distance $r^* \neq 0$ (Figure 4). At higher temperatures and distances $r^* \geq 1$ etching may even dominate (see curves for T_c = 2700 K and 3000 K). For even larger distances, the thickness of the deposit becomes finite again. Here, a thin film is formed via diffusion of atoms A out of the reaction zone. Further examples and details on the calculations can be found in (*6*).

Comparison with experiments. Figure 4 reveals that the transparent ring observed in Figure 1*a*' can be explained by etching, and the thin film by species generated within the gas phase. Additional calculations presented in (*6*) describe qualitatively the changes in spot shape mentioned in Sect.2. The hollow seen in Figure 4 near the center $r^* \approx 0$ is a consequence of the gas-phase transport limitation of species towards the reaction zone. Figure 5 may represent experimental evidence for such a behavior. The relative importance of deposition and etching reactions depends on the relative size of rate constants k_j. This, in turn, depends on the temperature, on the apparent activation energies ΔE_j, and on the

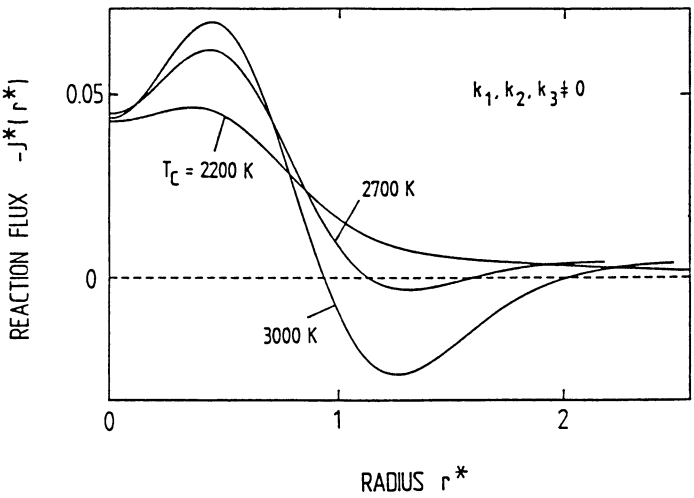

Figure 4. The normalized reaction flux as a function of r^* with $k_1 \neq 0$, $k_2 \neq 0$, $k_3 \neq 0$, $\Delta E_1/k_B$ = 15000 K, $\Delta E_2/k_B$ = 8000 K, $\Delta E_3/k_B$ = 10000 K. The different curves refer to T_c = 2200 K, 2700 K, 3000 K (Reproduced with permission from reference 6. Copyright 1992 Elsevier Sequoia).

partial pressures of species (these enter the preexponential factor k_{oj}).

The investigations summarized in this section permit the qualitative description of many features observed in pyrolytic laser-CVD. The main drawback in this type of approach is related to the assumption that the laser-induced temperature distribution remains unaffected during the deposition process. This can be considered, to some extent, as a reasonable approximation only as long as the thermal conductivities of the deposited material and the substrate are about equal (*1*).

4. Simulation of Growth

It has already been outlined in (*1*) that the laser-induced temperature distribution depends strongly on the geometry of the deposit. Therefore, any quantitative or semi-quantitative analysis of the deposition process requires a self-consistent treatment of the equation of growth and the laser-induced temperature distribution. In this section we present two models.

In paragraph 4.1 we employ a one-dimensional approach and we approximate the laser-induced temperature distribution by an analytic equation which is solved simultaneously with the equation of growth. This model can be applied to laser direct writing.

In paragraph 4.2 the equation of growth and the heat equation for the deposit are solved self-consistently for a two-dimensional model. Clearly, only numerical techniques can be employed in this case. Here, even with the assumption of a purely heterogeneous reaction and the omission of gas-phase transport, considerable computational efforts are required.

The type of approaches presented in this section ignore any gas-phase transport and assume a purely heterogeneous reaction. Nevertheless, they permit a semi-quantitative description of experimental data.

4.1 One-Dimensional Approach to Direct Writing. In this section we simulate pyrolytic direct writing in a one-dimensional self-consistent calculation.

The model employed in the calculations is depicted in Figure 6. It is applied to laser direct writing of a stripe (deposit) onto a semiinfinite substrate. The respective thermal conductivities and temperatures are denoted by κ_D, T_D and κ_S, T_S. Scanning of the laser beam is performed in x-direction with velocity v_s. We consider quasi-stationary conditions with the coordinate system fixed with the laser beam. Thus, in this system, the geometry of the stripe remains unchanged; its height behind the laser beam is h, and its width $d = 2r_D$. The temperature distribution induced by the absorbed laser-light intensity, I_a, is indicated by the dashed curve. Within the center of the laser beam at $x = 0$ the temperature is denoted by T_c, while at the forward edge of the stripe at $x = a$ it is denoted by T_e, and with $x \to -\infty$ by $T(\infty)$. As outlined in (*1*), changes in laser-induced temperature distribution related to changes in the

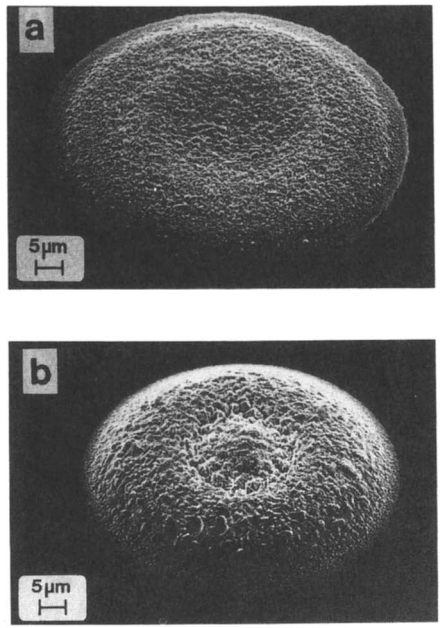

Figure 5. SEM pictures of W spots deposited from 0.49 mbar WCl_6 + 400 mbar H_2 by means of 680 nm dye-laser radiation a) P = 300 mW, τ_ℓ = 20 s b) P = 240 mW, τ_ℓ = 40 s (Reproduced with permission from reference 7. Copyright 1992 Elsevier Sequoia).

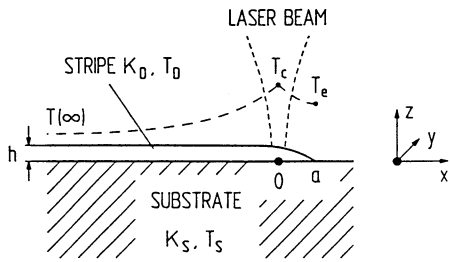

Figure 6. Schematic for direct writing. The coordinate system is fixed with the laser beam. The center of the laser beam with radius w is at the origin x = 0; the forward edge of the stripe is at x = *a*. T_c and T_e are the corresponding temperatures. The temperature profile is indicated by the dashed curve. The height of the stripe is h and its width is d = $2r_D$ (Reproduced with permission from reference 8. Copyright 1993 Elsevier Science Publishers B.V.).

geometry of the deposit are the more pronounced, the more the ratio of thermal conductivities differs from unity. For this reason we consider the case $\kappa^* = \kappa_D/\kappa_S >> 1$. This applies, for example, to direct writing of metal lines onto glass substrates. For further details on these calculations the reader is referred to (*8*).

4.1.1 Temperature Distribution. The laser-induced temperature distribution can be calculated from the energy balance

$$\kappa_D F \frac{\partial^2 T_D}{\partial x^2} - \eta \kappa_S \left[T_D - T(\infty) \right] + P_a \delta(x) = 0 \qquad (4.1)$$

and the boundary conditions

$$\left. \frac{\partial T_D}{\partial x} \right|_{x=a} = 0$$

$$T_D(x \longrightarrow -\infty) = T(\infty)$$

The first and the second term in (4.1) describe the transport of heat along the stripe and into the substrate, respectively. η is a dimensionless geometrical parameter. The source term is given by the absorbed laser power. The influence of scanning has been ignored. This is a good approximation as long as $v_s r_D^2/[D_s \ell] << 1$. D_s is the thermal diffusivity of the substrate, and ℓ some characteristic length (see below). All material parameters and the cross section of the stripe, $F \equiv F(x)$, have been assumed to be constants. Because $\kappa^* >> 1$ we ignore within the stripe any temperature gradient in y- and z-direction, i.e. $T_D(x,y,z) = T_D(x,0,0) \equiv T_D$ and set $T_S(z=0) \approx T_D$ The radius of the laser beam, w, was assumed to be small compared to r_D so that the absorbed laser power per unit length can be replaced by $P_a\delta(x) = PA\,\delta(x)$. A is the absorptivity. Finally, we introduce the variable

$$\ell^2 = \frac{F \kappa^*}{\eta} \qquad (4.2)$$

ℓ characterizes the drop in laser-induced temperature in x-direction. With $x < 0$ the solution of (4.1) is

$$T_D(x) = T(\infty) + \Delta T_c \exp\left[\frac{x}{\ell} \right] \qquad (4.3)$$

where

$$\Delta T_c \equiv \Delta T(x=0) = \frac{P_a}{2 \eta \kappa_S \ell} \left\{ 1 + \exp\left[- \frac{2a}{\ell} \right] \right\}$$

and with $0 < x < a$

$$T_D(x) = T(\infty) + \Delta T_e \cosh\left[\frac{x - a}{\ell}\right] \tag{4.4}$$

where

$$\Delta T_e \equiv \Delta T(x = a) = \frac{P_a}{\eta \kappa_s \ell} \exp\left[-\frac{a}{\ell}\right]$$

For the determination of the unknown quantities ΔT_c, ΔT_e, a, F, ℓ, h, and r_D we need four additional equations beside of (4.2)-(4.4). The cross section of the stripe is

$$F \approx \zeta\, h\, r_D \tag{4.5}$$

where ζ is a dimensionless geometrical coefficient ($\zeta \approx 2$ for a rectangular stripe, $\zeta \approx 4/3$ for a parabolic cross section, etc.). The width of the stripe is characterized by

$$r_D \approx \xi\, a \tag{4.6}$$

ξ is again dimensionless and of the order of unity. It determines the position of the laser beam. This Ansatz implies that the temperature distribution is approximately of axial symmetry near the tip of the stripe. This is confirmed by both experimental observations and more accurate numerical simulations of the growth process (see paragraph 4.2.2). We assume that the temperature at the tip of the stripe, T_e, is equal to the threshold temperature T_{th} at which deposition becomes significant (7), i.e. we set

$$T_{th} \approx \Delta T_e + T(\infty) \tag{4.7}$$

The fourth equation is given by (4.9).

4.1.2 Simulation of Growth. In a coordinate system that is fixed with the laser beam, the height of the stripe is given by

$$\frac{\partial h}{\partial t} = W(T_D) + v_s \frac{\partial h}{\partial x} \tag{4.8}$$

where $h = h(x,t)$. $W(T)$ is the growth rate as described by the Arrhenius law, $W(T) = k_o \exp[-\Delta E^*/T]$ where k_o [μm/s] is the preexponential factor and $\Delta E^* = \Delta E/k_B$ the apparent chemical activation energy. Clearly $\partial h/\partial x \neq 0$ only, if $W(T) \neq 0$, i.e. if $T > T_{th}$. Subsequently, we assume stationary conditions, $\partial h/\partial t = 0$. If we use for the position $x = 0$ the approximation $\partial h/\partial x \approx -h/[\gamma a]$ where h is now the (constant) height behind the laser beam, we obtain

$$W(T_c) - v_s \frac{h}{\gamma a} = 0 \qquad (4.9)$$

γ is again dimensionless and of the order of unity. Equations (4.2), (4.3-7), and (4.9) permit to calculate all relevant dependences.

From (4.1) and (4.9) we find that for constant v_s the lengths r_D, h, a, and ℓ scale linearly with the absorbed laser power, P_a. In this case T_c is independent of P_a. The dependence of these quantities on the velocity v_s is more complex. From (4.3) and (4.4) together with (4.7) we obtain

$$\mu = \frac{a}{\ell} = \text{arc cosh}\left[\frac{\Delta T_c}{\Delta T_{th}}\right] \qquad (4.10)$$

where $\Delta T_{th} = T_{th} - T(\infty)$. From (4.4) we find

$$\ell = \frac{P_a}{\eta \kappa_s \Delta T_{th}} \exp[-\mu] \qquad (4.11)$$

With (4.10) this yields

$$r_D = \xi a = \xi \ell \mu = \frac{\xi P_a}{\eta \kappa_s \Delta T_{th}} \mu \exp[-\mu] \qquad (4.12)$$

From (4.2), (4.5), and (4.6)

$$h = \frac{\eta}{\zeta \xi \kappa^*} \frac{a}{\mu^2} = \frac{P_a}{\zeta \xi \kappa_D \Delta T_{th}} \mu^{-1} \exp[-\mu] \qquad (4.13)$$

From (4.9) we obtain

$$v_s = \frac{\gamma \zeta \xi}{\eta} \kappa^* \mu^2 W(T_c) \qquad (4.14)$$

Equations (4.10) and (4.12-14) are a parametric representation for the determination of h and r_D as a function of v_s. Note, that both T_c and μ increase with v_s.

4.1.3 Comparison of Theoretical Results with Experimental Data. According to (4.12) and (4.13) the width and height of stripes produced by pyrolytic laser direct writing increases linearly with the laser power. This is in agreement with experimental data obtained with many different systems for which the model assumption $\kappa_D/\kappa_s >> 1$ holds (*1*).

The dependence of r_D and h on scanning velocity is more complicated. Figures 7 show the normalized quantities $h \kappa_D T(\infty)/P_a$ and

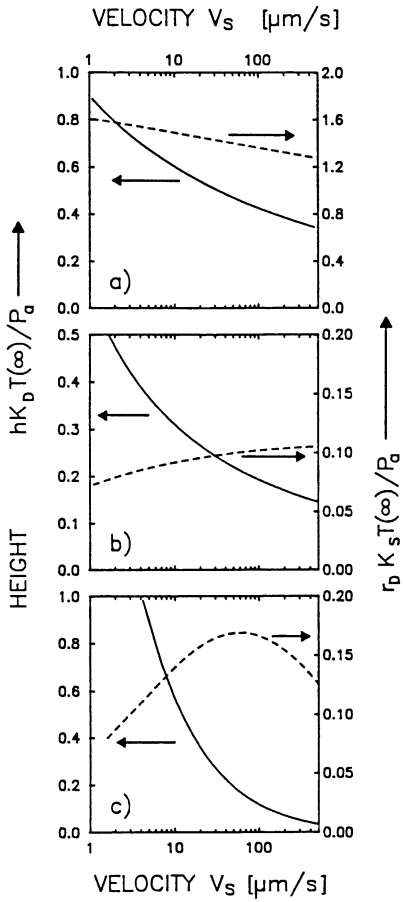

Figure 7. Normalized width and height of stripes as a function of scanning velocity. The respective parameter sets employed are in case *a*) $k_o = 5.3 \cdot 10^{12}$ μm/s, $\Delta E^*/T(\infty) = 45$, $T_{th}/T(\infty) = 1.17$, $\kappa^* = 30$; in case *b*) $k_o = 6.6 \cdot 10^9$ μm/s, $\Delta E^*/T(\infty) = 90$, $T_{th}/T(\infty) = 3.7$, $\kappa^* = 15$; and in case *c*) $k_o = 16.05$ μm/s, $\Delta E^*/T(\infty) = 5.7$, $T_{th}/T(\infty) = 2.7$, $\kappa^* = 17$. The geometrical factors are the same in all cases: $\eta = 1.6$, $\zeta = 4/3$, $\xi = 1.25$, and $\gamma = 1.3$ (Reproduced with permission from reference 8. Copyright 1993 Elsevier Science Publishers B.V.).

$r_D \kappa_s T(\infty)/P_a$ as a function of v_s, as calculated from (4.12-4.14). The respective parameter sets employed are listed in the figure caption. The figure shows that with all parameter sets, the height of stripes (full curves) decreases monotonously with increasing v_s. This is quite obvious, because the dwell time of the laser beam decreases with $1/v_s$. The width of stripes, $d = 2r_D$, shows a more complex behavior. In Figure 7*a*, r_D decreases monotonously with increasing scanning velocity, while in Figure 7*b* it increases monotonously. In Figure 7*c*, r_D first increases up to a maximum value r_D^{max}, which occurs at a velocity v_s^{max}, and then decreases for $v_s > v_s^{max}$. The different behavior can be understood from the fact that $r_D(v_s)$ shows a maximum at $\mu = 1$. For this point, we obtain

$$T_c^{max} = T(\infty) + \Delta T_{th} \cosh[1] \approx T(\infty) + 1.5\ \Delta T_{th}$$

$$r_D^{max} = \xi\, a = \xi\, \ell = \frac{\xi\, P_a}{\eta\, \kappa_s\, \Delta T_{th}}\, e^{-1} \qquad (4.12a)$$

$$h^{max} = \frac{P_a}{\zeta\, \xi\, \kappa_D\, \Delta T_{th}}\, e^{-1} \qquad (4.13a)$$

$$v_s^{max} = \frac{\gamma\, \zeta\, \xi}{\eta}\, \kappa^*\, W(T_c^{max}) \qquad (4.14a)$$

Thus, the different behavior shown in Figures 7*a-c* is related to the fact that the maximum in r_D can or cannot be observed within a reasonable range of scanning velocities, depending on the parameter set employed. For the material with the *low* deposition threshold (case *a*) the maximum velocity $v_s^{max} < 1\ \mu m/s$ and r_D will thereby decrease monotonously with increasing v_s. For a material with a rather high deposition threshold, r_D may increase monotonously with v_s (case *b*). Case *c* represents an intermediate situation. Qualitatively, the occurence of a maximum in $r_D(v_s)$ is related to the increase in T_c with increasing v_s. This increase in T_c, in turn, is related to the diminished heat flux along the stripe.

Let us now compare the behavior of $h(v_s)$ and $r_D(v_s)$ as shown in Figure 7 with experimental data.

The parameter set employed in the case of Figure 7*a* refers, approximately, to pyrolytic laser-CVD of Ni from $Ni(CO)_4$. In fact, experimental investigations on the direct writing of Ni lines have shown that r_D decreases with increasing scanning velocity (*1*).

The parameters employed for calculating the curves presented in Figure 7*b* describe, approximately, the deposition of Si from SiH_4 and of C from C_2H_2. For these systems, however, no systematic investigations on the direct writing of lines onto thermally insulating substrates are known.

The parameters employed in Figure 7*c* are typical for the deposition of W from $WCl_6 + H_2$ (*7*). The behavior shown in the figure is, in fact, in qualitative agreement with the experimental results obtained on the direct writing of W lines onto insulating substrates.

Subsequently, we compare the theoretical results with the experimental data obtained for direct writing of W lines deposited from $WCl_6 + H_2$ by means of cw Ar^+-laser radiation (λ = 514.5 nm; $w \equiv w_o(1/e)$ = 7.5 μm) onto quartz (SiO_2) substrates. The substrates employed in the experiments were frequently coated with a h_ℓ = 700 Å thick film of sputtered W. This film permits a well-defined initiation of the deposition process (*1*). Its influence on the temperature distribution can be ignored if $\kappa^* \cdot h_\ell / r_D << 1$. Other experimental examples and further details are outlined in (*1,2,7*).

Figure 8 shows experimental data for the height (squares) and width (triangles) of W stripes as a function of scanning velocity for two different WCl_6 pressures. The effective incident laser power was in both cases P = 645 mW. Full and dashed curves are calculated from (4.12-4.14) with the same geometrical factors as in Figure 7. The other parameters are noted in the figure caption. The height of stripes decreases with increasing velocity v_s. The width of stripes, however, first increases up to a maximum and then decreases with increasing v_s. As expected from (4.14a), the maximum value occurs at a higher velocity with the higher WCl_6 partial pressure. This is a consequence of the preexponential factor, k_o, in the reaction rate W(T). For a partial reaction order of unity with respect to the WCl_6 concentration, k_o is proportional to $p(WCl_6)$. This describes, at least qualitatively, the trend in the experimental results in Figures 8 to 10. Figure 9 shows the velocity v_s^{max}, corresponding to the maximum width as a function of laser power for $p(WCl_6)$ = 0.49 mbar (circles) and 1.1 mbar (squares). The figure shows that v_s^{max} increases by almost a factor of 2 to 3 when the WCl_6 pressure is increased from 0.49 mbar to 1.1 mbar. This is in qualitative agreement with (4.14a).

Equations (4.12a) and (4.13a) suggest that the maximum height, h^{max}, and width, d^{max}, depend only on threshold temperature and increase linearly with laser power. This is also confirmed by the experiments. Figure 10 shows the results for two different WCl_6 partial pressures. In fact, h^{max} and d^{max} show only a slight

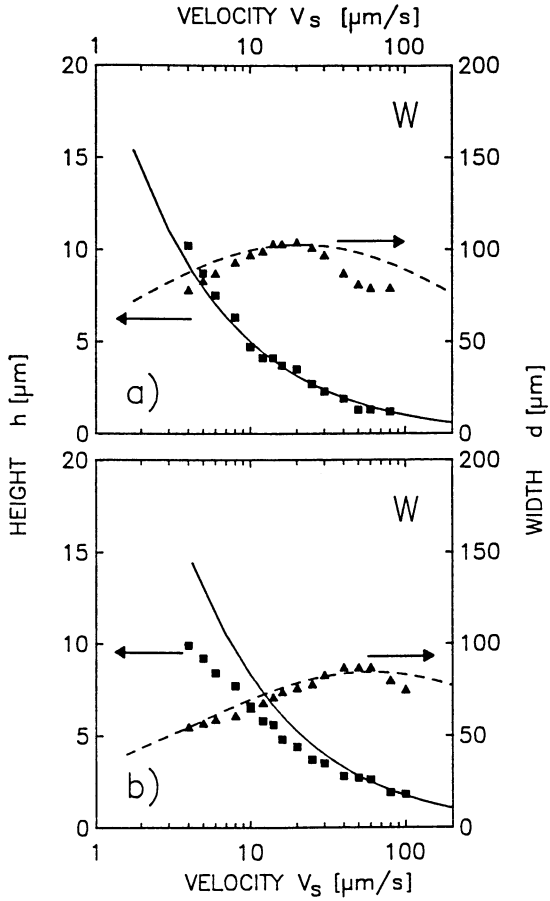

Figure 8. Width and height of W stripes as a function of scanning velocity for two mixtures of WCl_6 + H_2 . The H_2 pressure $p(H_2)$ = 50 mbar. The full and dashed curves have been calculated as described in the text. The parameters were P = 645 mW, A = 0.55, w_o = 7.5 μm, T(∞) = 443 K, $\Delta E^*/T(\infty)$ = 5.7, κ^* = 17, κ_s = 0.032 $Wcm^{-1}K^{-1}$; η = 1.6, ζ = 4/3, ξ = 1.25, γ = 1.3 a) $p(WCl_6)$ = 0.49 mbar, k_o = 7.15 μm/s, $T_{th}/T(\infty)$ = 2.4 b) $p(WCl_6)$ = 1.1 mbar, k_o = 16.05 μm/s, $T_{th}/T(\infty)$ = 2.7 (Reproduced with permission from reference 8. Copyright 1993 Elsevier Science Publishers B.V.).

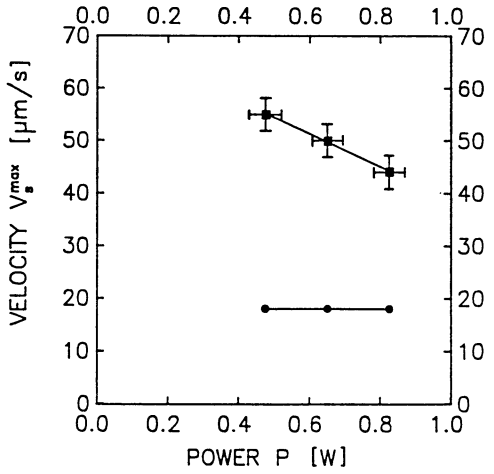

Figure 9. Scanning velocity v_s^{max} referring to the maximum width of stripes achieved in laser direct writing of W lines from WCl_6 + H_2 . The pressure was $p(H_2)$ = 50 mbar and ● $p(WCl_6)$ = 0.49 mbar, ■ $p(WCl_6)$ = 1.1 mbar (Reproduced with permission from reference 8. Copyright 1993 Elsevier Science Publishers B.V.).

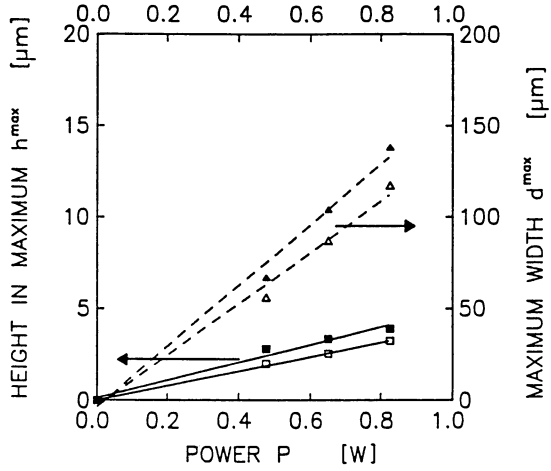

Figure 10. Maximum width and height of W stripes produced by laser direct writing from WCl_6 + H_2 . The H_2 pressure was $p(H_2)$ = 50 mbar. ■, ▲ $p(WCl_2)$ = 0.49 mbar ; □, Δ $p(WCl_2)$ = 1.1 mbar (Reproduced with permission from reference 8. Copyright 1993 Elsevier Science Publishers B.V.).

dependence on pressure. This can be understood from the (small) dependence of the threshold temperature on $p(WCl_6)$ (7).

With the approximations made in this model, the agreement between the theoretical predictions and the experimental data must be considered to be quite reasonable. Besides of the simplyfiing assumptions made, important parameters such as k_o, ΔE^*, and T_{th} can only be estimated from previous experimental investigations. This is true also for reaction orders. The temperature dependences in κ_D, κ_S, and A can be taken into account in a similar approach. Even in this case a linear dependence of r_D, h, *a*, and ℓ on absorbed laser power is predicted; the maximum center temperature, T_c^{max}, will still depend only on T_{th} and the materials' properties. With realistic parameters, the changes in quantities are smaller than 30%.

4.2 Two-dimensional model. Laser-CVD has also been simulated in a two-dimensional self-consistent calculation. The deposit is again placed on a semiinfinite substrate. The origin of the coordinate system is fixed with the laser beam. The shape of the deposit is described by an arbitrary function h(x,y) with $0 < z < h(x,y)$. As derived in (*9*), the temperature distribution can be calculated from

$$\theta_s(\theta_D) = \theta_s^o + \frac{\kappa^*(T(\infty))}{2\pi} \left\{ \nabla_2 \left[h \nabla_2 \theta_D \right] * \frac{1}{|\mathbf{r}|} \right\} \qquad (4.15)$$

where

$$\theta_s^o = \frac{1}{2\pi \kappa_S(T(\infty))} \left\{ I_a * \frac{1}{|\mathbf{r}|} \right\}$$

is the (linearized) temperature distribution without the deposit. θ_s and θ_D are the linearized temperatures for the substrate and the deposit, respectively. **r** is a two-dimensional radius vector within the xy-plane, and * denotes the convolution integral. With (4.15) the shape of the deposit can be calculated from (4.8). Further details on the model calculations and their applications can be found in (*9*).

In the following we will present only some results on the simulation of growth of W and Ni spots and on the direct writing of W lines. The substrate material considered is quartz (SiO_2).

For convenience, we introduce normalized quantities and indicate them by an asterisk. h, x, y, v_s, and k_o are normalized to the radius of a Gaussian laser beam, w_o. Correspondingly, all temperatures and activation energies are normalized to the temperature $T(\infty)$. The normalized maximum intensity is $I_o^* = I_o w_o / [T(\infty)\kappa_S(T(\infty))]$.

4.2.1 Growth of Spots. Figure 11 shows the (normalized) height of W spots calculated for various stages of growth as a function of the (normalized) distance from the center of the laser-beam. The kinetic data employed, $k_o^* = 2.14$, $\Delta E^* / T(\infty) = 5.68$, were taken from experimental investigations on the deposition of W from $WCl_6 + H_2$ (7). The other parameters used were $T_{th} / T(\infty) = 2.71$, $\delta T_{th} / T(\infty) = 0.01$, $\kappa^*(T(\infty)) = 50.56$, $AI_o^* = 10.3$. δT_{th} characterizes the sharpness of the threshold. The thermal conductivity of the deposited W is approximated by $\kappa_D(W) = c_1 + c_2/T - c_3/T^2$ where $c_1 = 42.65\ Wm^{-1}K^{-1}$, $c_2 = 1.898 \cdot 10^4\ Wm^{-1}$ and $c_3 = 1.498 \cdot 10^6\ Wm^{-1}K$. This corresponds to one half of the heat conductivity reported in (*10*)]. For the SiO_2 substrate we choose $\kappa_s(SiO_2) = a_1 + a_2T$ with $a_1 = 0.9094\ Wm^{-1}K^{-1}$ and $a_2 = 1.422 \cdot 10^{-3}\ Wm^{-1}\ K^{-2}$ (*11*). The Kirchhoff transform permits to find the approximations

$$\theta_s^* \approx \theta_D^* + 0.46\ \theta_D^{*2}$$

and

$$T_D^* \approx 1 + \theta_D^* + 0.12\ \theta_D^{*2}$$

The accuracy of this approximation within the temperature interval $T(\infty) = 443\ K \leq T_D \leq 2500\ K$ is 2 - 3 %.

Figure 11 demonstrates the very fast spreading of the deposit in lateral direction. The velocity of lateral growth is strongly influenced by the width of the threshold, δT_{th}. The saturation in spot diameter, which occurs when the temperature near the edge of the spot becomes smaller than the threshold temperature for deposition, is in agreement with experimental observations (7). It becomes evident that the saturation in width takes place much faster than the saturation in height. The change in the (normalized) temperature distribution during the growth process is shown in the lower part of the figure. It shows that within a short time the surface temperature becomes almost uniform over the surface of the spot.

Figure 12 shows the growth of Ni spots deposited from $Ni(CO)_4$. In this case the thermal conductivity of the deposited Ni and of the substrate was kept constant with $\kappa^*(T(\infty)=300\ K) = 30$. The other parameters employed in the calculations were $T(\infty) = 300\ K$, $k_o^* = 1.1 \cdot 10^{13}$, $\Delta E^* / T(\infty) = 45$ and $AI_o^* = 1.33$. Here, no threshold was assumed so that $T_{th} / T(\infty) = 1$. The kinetic parameters correspond to the pyrolytic decomposition of $Ni(CO)_4$ (*1*). Due to the absence of a threshold, there is no abrupt saturation in the width of the Ni spots. Furthermore, the ratio of spot height to spot width is much larger than in the case of W. This is related to the much higher

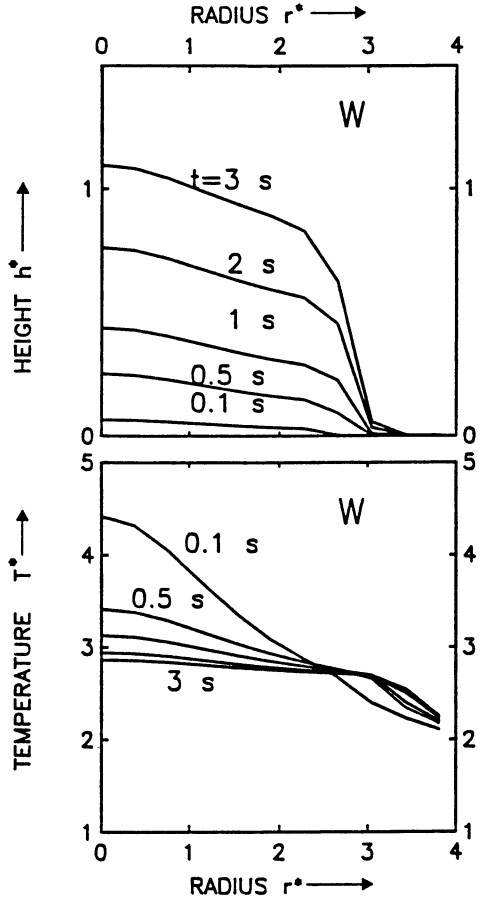

Figure 11. Normalized height of W spots calculated for various stages of growth as a function of the (normalized) distance from the laser-beam center. The parameters employed are typical for laser-CVD of W from WCl_6 + H_2 (see text). The lower part of the picture shows the evolution of the (normalized) surface temperature distribution (Reproduced with permission from reference 9. Copyright 1993 Elsevier Science Publishers B.V.).

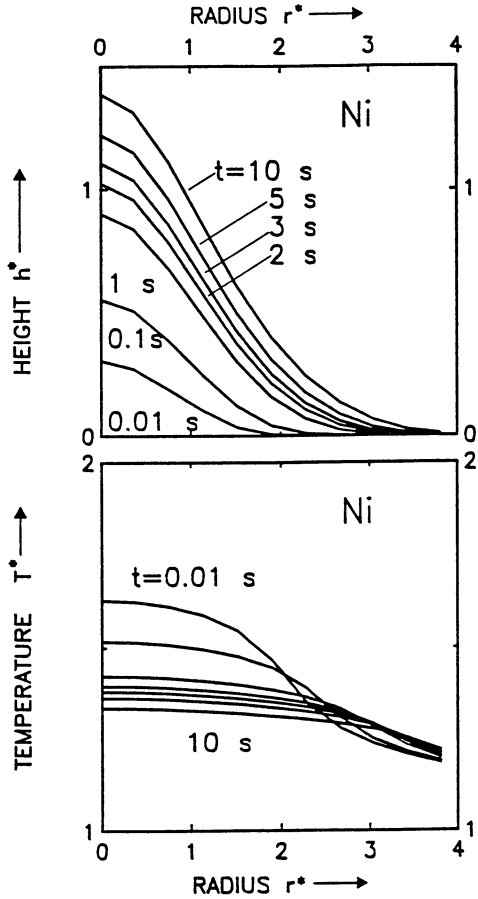

Figure 12. Same as Figure 11 but for Ni spots deposited from $Ni(CO)_4$ (Reproduced with permission from reference 9. Copyright 1993 Elsevier Science Publishers B.V.).

activation energy, ΔE^*; it yields a significantly higher growth rate in the center than near the spot edge. This behavior is in qualitative agreement with experimental observations (*1,12*). The change in temperature distribution related to the growth of the spot is similar to that oberved for W.

4.2.2 Direct writing of lines. Figure 13 shows contour lines (left side) and isotherms (right side) calculated for various stages of direct writing of W lines deposited from $WCl_6 + H_2$. The laser beam is switched on at time t = 0. The scanning velocity employed was $v_s^* = 2.0$, the absorbed laser-beam intensity $AI_o^* = 20.6$. The other parameters are the same as in Figure 11. The figure shows that the stationary solution is achieved only after a rather long time. The larger width of the stripe observed in the initial phase of growth (short times) is related to the fact that energy losses due to heat conduction along the stripe are not yet effective. This behavior becomes evident also from the isotherms. It is in agreement with experimental observations.

Within the regime of parameters investigated, the shape of the calculated W stripes remains always uniform, i.e. shows no oscillations in height or width (*1*).

Calculations of the kind presented in Figure 13 permit to derive the parameter $\xi = r_D/a$ for different scanning velocities [see also (4.6)]. From these calculations we find $1.2 < \xi < 1.5$. Experimentally we find for the $WCl_6 + H_2$ system $\xi \approx 1.25$.

The calculations performed in (*9*) show that the discrepancy between the model presented in Sect. 3.2 and the present model is about 30% within the range of reasonable parameters.

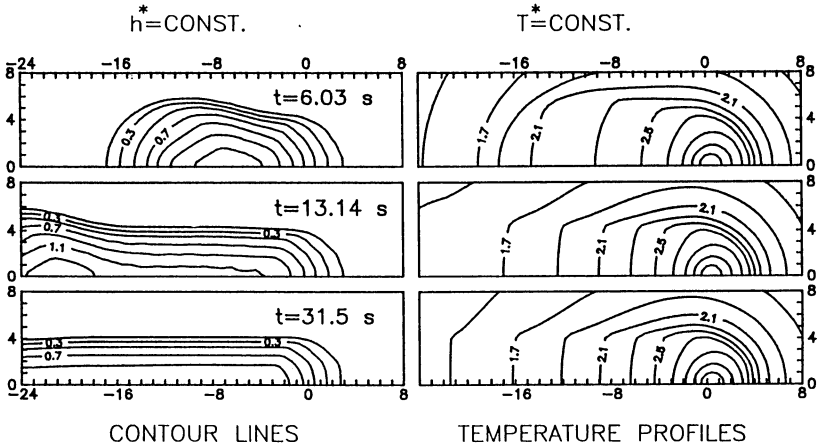

Figure 13. Contour lines (left side) and isotherms (right side) calculated for W stripes produced by laser direct writing. The laser beam is switched on at t = 0 (Reproduced with permission from reference 9. Copyright 1993 Elsevier Science Publishers B.V.).

5. Conclusion

Theoretical models on the gas-phase kinetics and the simulation of growth permit to explain many features observed in pyrolytic laser-CVD of microstructures. Such calculations together with experimental data allow an optimization of the deposition process with respect to specific applications.

Acknowledgement: We wish to thank the "Fonds zur Förderung der wissenschaftlichen Forschung in Österreich" for financial support.

Literature Cited:

(*1*) Bäuerle, D. *Chemical Processing with Lasers*; Springer Series in Materials Science; Springer: Berlin, Heidelberg, 1986; Vol. 1.
(*2*) Toth, Z.; Kargl, P.B.; Grivas, C.; Piglmayer, K.; Bäuerle, D. *Appl. Phys. B* **1992**, 54, 189.
(*3*) Bäuerle, D.; Luk'yanchuk, B.; Piglmayer, K. *Appl. Phys. A* **1990**, 50, 385.
(*4*) Kirichenko, N.; Piglmayer, K.; Bäuerle, D. *Appl. Phys. A* **1990**, 51, 498.
(*5*) Luk'yanchuk, B.; Piglmayer, K.; Kirichenko, N.; Bäuerle, D. *Physica A* **1992**, 189, 285.
(*6*) Kirichenko, N.; Bäuerle, D. *Thin Solid Films* **1992**, 218, 1.
(*7*) Kullmer, R.; Kargl, P.; Bäuerle, D. *Thin Solid Films* **1992**, 218, 122.
(*8*) Arnold, N.; Kullmer, R.; Bäuerle, D. *Microelectronic Engineering* **1993**.
(*9*) Arnold, N.; Bäuerle, D. *Microelectronic Engineering* **1993**.
(*10*) *Handbook of Chemistry and Physics*; Weast, R.C., Ed.; 59th ed. CRC Press: Boca Raton, FL, 1978/79.
(*11*) Heraeus Inc., Germany: data sheet Q-A 1/112, 1979.
(*12*) Piglmayer, K.; Bäuerle, D. In *Laser Processing and Diagnostics II*; Bäuerle, D.; Kompa, K.L; Laude, L.D., Eds.; Les Editions de Physique: Les Ulis 1986), pp 79-84.

RECEIVED April 1, 1993